Title

Composite Laminate Fatigue Damage Detection and Prognosis Using Embedded Fiber Bragg Gratings

Authors

Todd, Michael
Gregory, William
Key, Christopher
et al.

Publication Date

2018-09-10

DOI

10.1115/smasis2018-8182

Peer reviewed

Proceedings of the ASME 2018 Conference on Smart Materials, Adaptive Structures and Intelligent Systems
SMASIS2018
September 10-12, 2018, San Antonio, TX, USA

SMASIS2018-8182

Composite Laminate Fatigue Damage Detection and Prognosis Using Embedded Fiber Bragg Gratings

Dr. Michael Todd
Department of Structural Engineering, University of California San Diego, La Jolla, CA 92093-0085 USA

William Gregory
Applied Physical Sciences Corporation Groton, CT 06340-3780 USA

Christopher Key
Applied Physical Sciences Corporation, Groton, CT 06340-3780 USA

Dr. Michael Yeager
vScenario San Diego, CA USA

Jordan Ye
Department of Structural Engineering, University of California San Diego, La Jolla, CA 92093-0085 USA

ABSTRACT

In many structural applications the use of composite material systems in both retrofit and new design modes has expanded greatly. The performance benefits from composites such as weight reduction with increased strength, corrosion resistance, and improved thermal and acoustic properties, are balanced by a host of failure modes whose genesis and progression are not yet well understood. As such, structural health monitoring (SHM) plays a key role for in-situ assessment for the purposes of performance/operations optimization, maintenance planning, and overall life cycle cost reduction. In this work, arrays of fiber Bragg grating optical strain sensors are attached to glass-epoxy solid laminate composite specimens that were subsequently subjected to specific levels of fully reversed cyclic loading. The fatigue loading was designed to impose strain levels in the panel that would induce damage to the laminate at varying numbers of cycles. The objectives of this test series were to assess the ability of the fiber Bragg grating sensors to detect fatigue damage (using previously developed SHM algorithms) and to establish a dataset for the development of a prognostic model to be applied to a random magnitude of fully reversed strain loading. The prognostic approach is rooted in the Failure Forecast Method, whereby the periodic feature rate-of-change was regressed against time to arrive at a failure estimate. An uncertainty model for the predictor was built so that a probability density function could be computed around the time-of-failure estimate, from which mean, median, and mode predictors were compared for robustness.

INTRODUCTION

Glass reinforced plastic (GRP) composite material systems are becoming increasingly desirable for high-performance marine structures, for both backfit and new design, because of their attractive strength/stiffness properties and corrosion resistance, among other properties. One of the disadvantages offsetting these performance benefits is the existence of failure modes (e.g., delamination, disbonding, fiber breakage, matrix cracking, and bearing damage in connections) which do not always have correlated visual damage indicators and do not have well-established failure genesis or historical data records. Methods of damage assessment like ultrasonic testing (UT) are costly and require that the structure be removed from service; in addition, these methods do not provide insight into the real-time onset and progression of the damage during operations. As such, structural health monitoring (SHM) systems offer the opportunity to play a key role for in-situ assessment for the purposes of performance/operations optimization, maintenance planning, and overall life cycle cost reduction.

This work employs a network of surface mounted fiber Bragg gratings (FBG) in a passive sensing approach to detect vibration-based fatigue damage onset and progression. Thorough reviews of vibration-based SHM have been performed by other researchers over many years. Passive sensing systems rely on ambient excitation of the structure and, therefore, generally assume that the input is unknown or otherwise immeasurable. The technical literature presents several successful implementations of passive damage

detection systems using a variety of sensing modalities and damage sensitive features[1-3]. Fiber Bragg gratings, in particular, are an attractive sensing choice because of several advantages over traditional strain sensors including; light weight, corrosion resistance, impermeability to liquid absorption, immunity to electromagnetic interference, and the ability to be multiplexed on a single fiber[4-7]. Although several studies have been performed regarding the use of optical sensors in the health monitoring of composites [7-9], larger-scale dense deployments are quite rare in the literature. This work attempts to bridge this gap by discussing data acquisition, feature extraction, and decision making within a simulated damage detection scenario using FBGs to measure the strain response in a composite panel subjected to fatigue induced damage. Thus, the full "data-to-decision" implementation of SHM is presented.

NOMENCLATURE

FBG – Fiber Bragg Grating
FE – Finite Element
GRP – Glass Reinforced Plastic
SHM – Structural Health Monitoring

UT – Ultrasonic Testing

APPROACH

A testing program was designed and executed to demonstrate the ability of a structural health monitoring (SHM) system utilizing fiber Bragg grating (FBG) sensors to detect damage in a glass-reinforced plastic (GRP) laminate due to fatigue loading in a composite structure. Two key questions were examined:

- Would the FBG sensors survive the fatigue environment under fully reversed loading and maintain functionality during the testing?
- Would the SHM algorithm developed and presented in [10] during impact loading be transportable to detect damage in a fatigue loading environment?

Assuming a positive answer to the above questions, the tests were executed to collect the sensor response data necessary to build and validate a damage prognostics algorithm for GRP laminates under fully reversed loading.

TEST DESIGN AND PROCEDURE

Test Approach

To collect the necessary FBG sensor response, a fatigue test approach was developed to obtain the response at strain levels that would represent elastic/no damage and damage response. In designing the test series, finite element (FE) analyses were conducted to establish strain levels for each specimen. The test approach was to load multiple specimens, each at specific strain targets. One specimen was designed to remain undamaged over the entire fatigue cycle range. A second specimen was designed to exhibit minimal damage, and a third was designed to exhibit fatigue damage. The definition of damage was based on an observable change in the specimen response as quantified by the accelerometers mounted on each specimen. An undamaged specimen would exhibit no change in the specimen response, as indicated by the accelerometer data; a damaged specimen would experience a change in properties (due to matrix level damage) and exhibit a change in the response as indicated by the accelerometer data.

A target of 1,000,000 cycles (maximum) for the testing duration was set in order to establish strain levels. ASTM level component test results of the glass-epoxy prepreg material were used to define target strain levels that would result in fatigue damage in the range of 750,000 to 1,000,000 cycles. The test data indicated that fully reversed strain levels of approximately 4800 με would exhibit failure at 100,000 cycles and strain levels of approximately 3700 με would exhibit failure at 1,000,000 cycles.

To obtain the response, a 4-point bend GRP specimen was loaded in a fully reversed bending manner by driving the specimen on a vibration table at a targeted vibratory frequency to obtain the strain response levels. Finite element analysis was conducted to size the test article, design the test fixture and set the testing parameters to obtain the targeted strain levels.

Finite Element Analysis

A finite element (FE) model of the test specimen geometry was developed and subjected to a forced vibration response study to determine the appropriate combination of load frequency and dummy mass to achieve the targeted strain levels. Figure 1 shows an example of the strain contour plot of one of the specimens resulting from the FE analysis. As shown, the ε11 strain (along the length of the specimen) at the mid-span is approximately 2900 με with peak strains near the clamping fixture on the order of 4600 με.

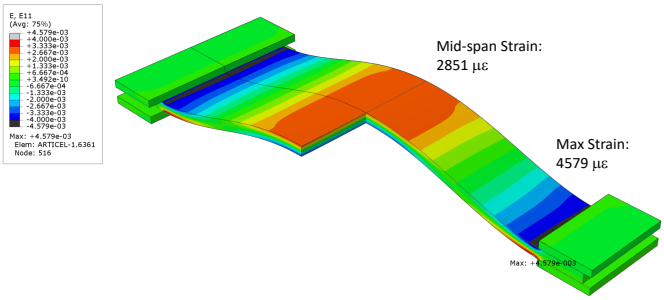

Figure 1. FE Strain Plot - Example

Various combinations of dummy mass and panel support length were modeled and analyzed to find the appropriate combination to reach the target strain levels for elastic/no damage and damage response. Figure 2 shows the frequencies

associated with each of the tested specimens versus the testing frequency. The approach taken to obtain the desired strain levels was to determine an appropriate dummy mass to drive each specimen "close" to resonance based on each panel's fundamental frequency. For example, Panel3C was determined to have a frequency of approximately 17.4, while being driven at 15.75 Hz, resulting in the desired strain level in the panel.

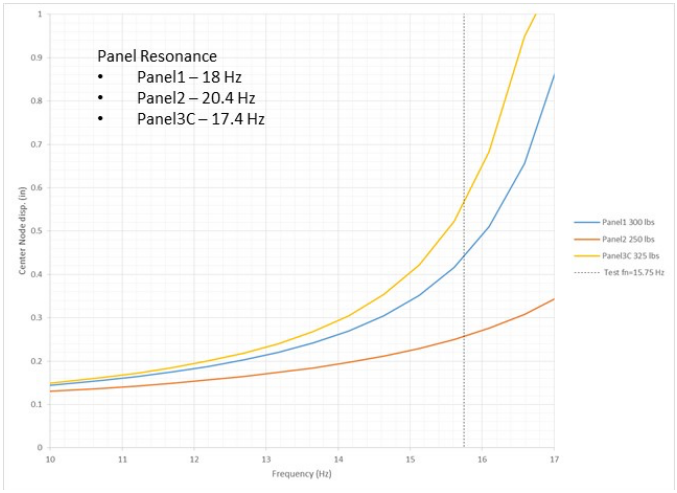

Figure 2. 4-Pt Bend Panel Frequencies

Test Specimen

A solid laminate, uniform thickness panel was designed and fabricated for the test series. The panel specimens were fabricated by United Technologies Aerospace Systems (UTAS) in Jacksonville, Fl. using glass-epoxy prepreg. The specimens were each 10" wide by 32" long with a target thickness of 0.6875" (to represent a full thickness part that may be employed in an application).

Post fabrication, twelve (12) FBG sensors from Alxenses were installed on the surface of the panel.. Design requirements for the sensor arrays included specifying the wavelength for each FBG sensor as well as the distance between sensors to mitigate possible fiber crimping issues with the layout. The locations of the sensors were defined using the FE strain contour plots, such that all sensors were positioned to collect unique strain data and levels during the test. All of the sensors were oriented in the longitudinal direction (long direction) of the specimen. The final locations of all 12 sensors are identified in Figure 3 (circled in RED).

Prior testing under this program [10] has shown that embedding the FBG sensors is achievable and in the actual application, will be necessary; however, for this test series, the sensors were surface mounted to facilitate data collection.

Figure 3. FBG Array Layout

Test set-up

As noted above, the test specimen were subjected to a constant fully reversed loading via a vibration table. Figure 4 shows the test set-up, where three specimen were simultaneously tested to specific strain levels. The figure shows the specimens mounted to the fixture prior to the installation of the dummy mass. Dummy mass was bolted to the specimens to simulate a 4-pt bending response, as dictated by the finite element (FE) analysis. Figure 5 shows the specimens mounted to the test fixture with dummy masses installed. The specimens included the following dummy mass configurations:

- Panel1 – 300 lbs. Matrix Damage expected; up to 1,000,000 (strains up to 4000 microstrain)
- Panel2 – 250 lbs. No Damage up to 1,000,000 cycles (strains in the 2000 – 2500 microstrain range)
- Panel3C – 325 lbs. Low Cycle Damage expected prior to 200,000 cycles (strains up to 5000 microstrain)

Figure 4. Test Specimens Bolted onto Test Fixture

Figure 5. Test Specimens with Dummy Mass

Accelerometers were mounted on each of the dummy masses along with accelerometers on the base on the test fixture. Figure 6 shows an accelerometer mounted to Panel1 dummy mass. This instrumentation was used to monitor the change in the panel response during the testing. Comparing the dummy mass accelerometer data vs. the fixture provided a mechanism to observe the relative motion between the two locations; change in the relative motion was an indicator used to determine if the specimen had experienced damage.

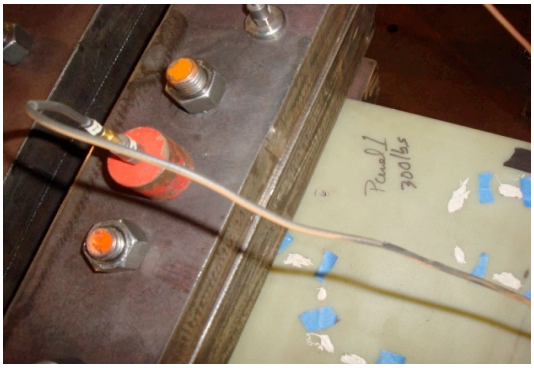

Figure 6. Accelerometers Mounted onto the Dummy Mass

Test Procedure

At the beginning of the test series, each panel was visually inspected and subjected to a shaker test. An electromechanical shaker, suspended from above the panel, was used to establish a baseline response for the FBG sensors, see Figure 7. The shaker was powered with an MB Dynamics power amplifier and provided a simulated pseudorandom excitation.

The fatigue testing was stopped and the dummy masses removed at discrete intervals to perform a visual inspection and also to conduct interim shaker excitations to characterize each of the panel specimens during the fatigue process. The shaker was attached to the panel and actuated for 2 minutes with band-limited white noise (BLWN). The excitation signal ranged from 10 Hz to 2500 Hz. The upper bound was governed by the Nyquist sampling limitations of the optical interrogation hardware and the lower bound was selected to exclude very low frequency components near the oscillation frequency of the suspended shaker. Each 120-second time history was windowed and segmented into 2-second tests for a total of 58 individual tests at each of the 12 discrete damage levels.

Figure 7. Electromagnetic Shaker Set-up

RESULTS

In all SHM implementations, cleansed data must be mined for damage sensitive features. The ideal feature is a quantity that changes as damage is introduced into the structure but is minimally affected by changes to the operational environment. For this exercise, the cross-power spectral density (CPSD) estimate was used as the foundational space for feature mining. The CPSD is defined as

$$\hat{S}_{ij} = \frac{2}{N} E\left[X_i^*(\omega) X_j(\omega) \right], \tag{1}$$

where the $E[\ ]$ operator signifies an ensemble average of the Fourier transforms $X_i(\omega)$ and $X_j(\omega)$. From this definition, it is evident that the quantity will be maximally correlated at global structural resonant maxima. The prominent peaks are selected from the CPSD and their shifts were tracked as a multivariate feature set i.e.,

$$\mathbf{x} = \begin{bmatrix} \Delta_1 & \Delta_2 & \dots & \Delta_k \end{bmatrix} = \left[\arg\max\left(\hat{S}_{ij}^{b}\left[\omega_{0,k}\right] \right) \right] - \left[\arg\max\left(\hat{S}_{ij}^{u}\left[\omega_{u,k}\right] \right) \right], \quad (2)$$

where $\hat{S}_{ij}^{b}$ and $\hat{S}_{ij}^{u}$ represent the CPSDs for the i^{th} and j^{th} sensor for the baseline and unknown structural states respectively. The frequency values $\omega_{0,k}$ and $\omega_{u,k}$ are the arguments that maximize $\hat{S}_{ij}^{b}$ and $\hat{S}_{ij}^{u}$ respectively. Finally, this multivariate feature set was reduced to a scalar distance metric, the Mahalanobis distance, by

$$D_i = \left(\mathbf{x}_i - \bar{\mathbf{x}}\right)^T \Sigma^{-1} \left(\mathbf{x}_i - \bar{\mathbf{x}}\right) \quad (3)$$

where $\mathbf{x}_i$ is a feature vector for an unknown structural state, $\bar{\mathbf{x}}$ is the mean of feature vectors from the baseline training set, and Σ is the covariance matrix of the baseline training set.

Recall that there are 58 individual 2-second tests across the 12 sensors. Because sensor pairs were used to generate the damage sensitive features, we have 66 unique sensor pairings. The plot shown in Figure 8 presents the Mahalanobis distances for representative sensor pairs at the discrete damage levels as a function of test number.

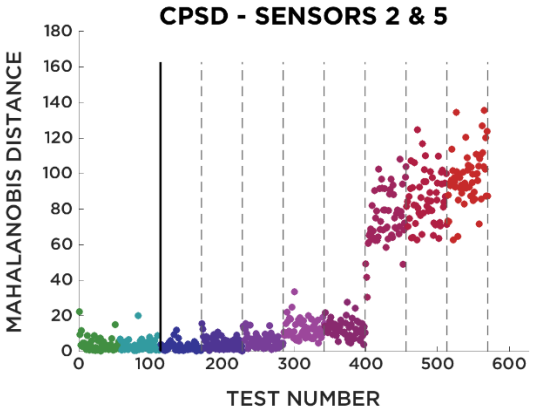

Figure 8. Mahalanobis Distances for Representative Sensor Pair

In this plot, the data points to the left of the solid black line are the baseline (undamaged) distances and the data between the dashed lines are the distances collected at different damage accumulation levels. It is clear that as fatigue is accumulated in the structure, the feature responds in a correlative manner.

The aforementioned plot does not, however, introduce any notion of time. So if these Mahalanobis distributions are plotted along with cycle count, we can see the feature change as a function of time. This idea of "feature rate" is ultimately the basis for the prognostics model. Figure 9 shows a plot of Mahalanobis distance vs. cycle count for Pane3C. Around the 100,000 cycle count, noticeable matrix damage was observed on Panel3C; at that test stop, minor change in the metric was observed. Between 100,000 and 125,000, the plot of the Mahalanobis distance indicates a change in the response, which continues to increase up to the 137,000 cycle count test stoppage. The change in the metric from 137,000 to 152,000 indicates continued damage to the specimen.

To accompany that plot, a plot of the two accelerometers on the dummy masses are shown in Figure 10. In addition to the specimen accelerometer data, the table accelerometer data is provided. It should be noted that the table provides a constant accelerometer reading throughout the test while the specimen accelerometer shows changes as damage initiates and progresses. At approximately 100,000 cycles, the accelerometer plot shows a change occurring in the panel response, as noted by the change in slope of the plot (i.e., accelerometer readings are increasing with cycle count). The specimen response continues to change, leading to a dramatic change in response near 140,000 with test completion at 152,000. It is noted that the test was stopped prior to complete catastrophic failure of the specimen.

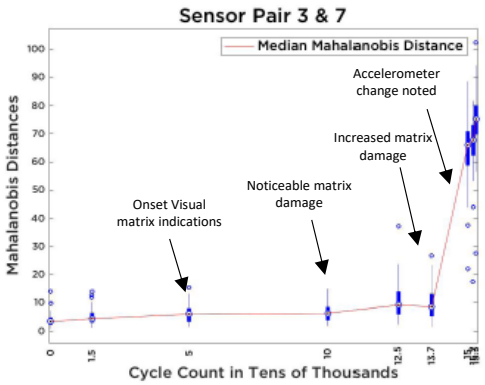

Figure 9. Mahalanobis Distances for Representative Sensor Pair vs. Cycle Count – Panel3C

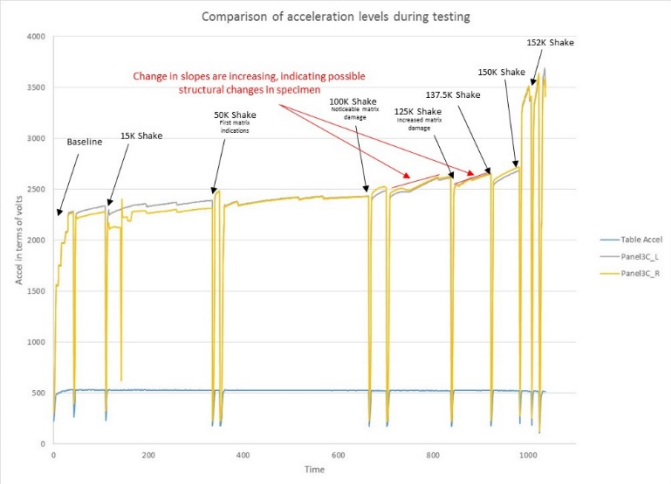

Figure 10. Accelerometer Data - Panel3C

For comparison to the plots for Panel3C, a plot of the Mahalanobis distance for Panel1 is shown in Figure 11. As shown in this figure, up to approximately 250,000 cycle there were no changes observed in the tracked metric. At approximately 350,000, there were visual indications of matrix damage, which continued to increase in intensity until the end of the test. At that same cycle count, the Mahalanobis distance began to show subtle changes which accompanied the visual determination of matrix damage.

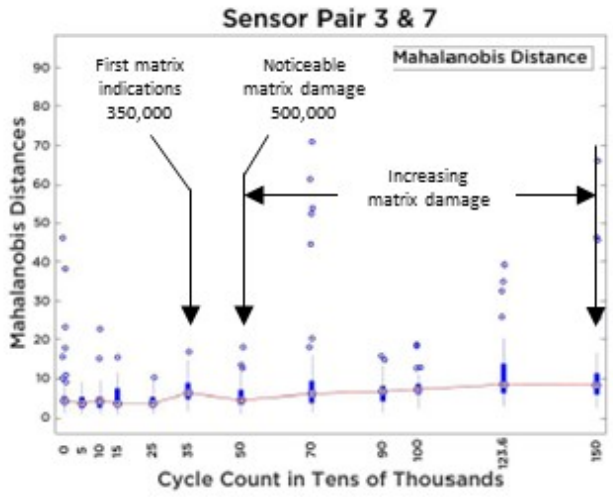

Figure 11. Mahalanobis Distance vs. Cycling (0 to 1,500,000 Cycles) – Panel1

PROGNOSTICS

Predictive modeling generally takes two broad forms: physical model-based or data model-based. For complex failure scenarios in complex structural geometries such as the present case of composite material systems fatigue, physical models are difficult to build due to the vast uncertainties in the (large number of) model parameters. Conversely, it has been observed empirically that a wide variety of failure mechanisms (ranging from earthquakes, volcanic eruptions, creep, fatigue, etc.) have a "self-accelerating" property; that is, the rate of change in some observed feature (anything from a raw measurement, such as strain, to something derived from the raw measurement) is strictly positive-valued with a positive derivative. This observation was generalized and formulated into a more comprehensive empirical model by Voight [11], known as the Failure Forecast Method, which has been applied to and adapted for a large number of geophysical and material-level failure mechanisms [12-16]; the universal feature of the approach is that the time of "failure" is self-defined by a positive feedback mechanism leading to (mathematically) an infinite value in the rate-of-change of the observed feature [17]. Of course, in any such empirical model, there are uncertainties associated with (at minimum) the observed data/features, rendering such a prediction stochastic. It is this approach that the current work will follow.

The failure forecast method empirical model proposes that the time rate-of-change R in some feature Ω, e.g., $R = \dot{\Omega}$, obeys an equation of the form

$$\dot{R} = kR^{\alpha}, \tag{1}$$

where $k > 0$ and $\alpha > 1$ are empirical constants. The solution to Eq. (1), assuming that the rate R at the time of failure t_f is R_f, is given by

$$R(t) = \left(R_f^{1-\alpha} + k\left(\alpha - 1\right)\left(t_f - t\right)\right)^{\frac{1}{1-\alpha}}. \tag{2}$$

The most common implementation considers the inverse of the rate R, since this facilitates easier definition of the failure criterion, i.e., the inverse rate tends to zero as the rate itself becomes infinite at the time of failure. Defining the inverse rate, $P = R^{-1}$, the solution Eq. (2) has the same exact form with $1-\alpha \Rightarrow \alpha - 1$, from which the time of failure may be obtained as

$$t_f = t + \frac{P^{\alpha-1} - P_f^{\alpha-1}}{k\left(\alpha - 1\right)}. \tag{3}$$

Thus, the time of failure is predicted to be the current time plus the proportional difference between the $(\alpha-1)$-th power of the current observed inverse rate data, $P^{\alpha-1}$, and the same power of the target inverse failure criterion. The approach is then to perform a regression on Eq. (3), which can be rearranged to give

$$\frac{P^{\alpha-1}-P_f^{\alpha-1}}{\alpha-1}=kt_f-kt. \tag{4}$$

If α is known or assumed, regression coefficients obtained from a time/data linear regression (over some given window of time) are given by $\beta_0=kt_f$ (intercept) and $\beta_1=-k$ (slope) such that the regression-estimated time to failure is $\hat{t}_f=-\beta_0/\beta_1$, or the negative of the ratio of the estimates of the intercept to the slope. If α is not known, a maximum likelihood estimation technique could be used. This works exploits that, based on historical observations in many of the cited studies above, regardless of the physical process, $\alpha\approx 2$, so that Eq. (4) is a simple linear regression. The "idealized" target failure criterion is that $P_f=0$, corresponding to $R_f\to\infty$; by setting it to any (positive) non-zero amount, a degree of conservatism is introduced into the approach. Of course, in most practical applications, "failure" occurs at a point prior to an infinite data rate-of-change observation, but to be consistent with general implementation in the literature and for the purposes of parametric studies in this paper, we will employ $P_f=0$ as the failure criterion, which won't change the basic nature of this study.

Any given regression on a data set represents a "single block" observation over some time interval, which is presumed representative of an ensemble population of regressions over the same time frame under inevitable noise and uncertainty. Thus, the regression coefficient estimates $\boldsymbol{\beta}=\left[\hat{\beta}_0,\hat{\beta}_1\right]^T$ are estimates from populations of regression coefficients. For a given linear regression model $\mathbf{P}=\mathbf{T}\boldsymbol{\beta}+\mathbf{e}$, where $\mathbf{P}$ is the data, $\mathbf{T}$ is the design matrix, and $\mathbf{e}$ is the regression error, it is assumed that the regression process yields errors that are unbiased, uncorrelated normal $\mathbf{e}\sim N\left(\mathbf{0},\sigma^2\mathbf{I}\right)$ under typical central limit theorem assumptions (regardless of the distribution in the regressed data, $\mathbf{P}$). Thus, it is known that the regression coefficients themselves have jointly normal distributions $\hat{\beta}_j\sim N\left(\beta_j,\sigma^2\left(\mathbf{T}^T\mathbf{T}\right)^{-1}\right)$, j=0,1. An unbiased estimate of the population error variance is $\sigma^2=\left\|\mathbf{P}-\mathbf{T}\hat{\boldsymbol{\beta}}\right\|^2/\left(n-2\right)$, where n is the number of data points used in the regression design, reduced by two since two regression coefficients were estimated in the process.

Given the uncertainty models in the regression coefficients, the time-of-failure is given by $\hat{t}_f=-\hat{\beta}_0/\hat{\beta}_1$, the ratio of our two normally-distributed regression coefficients. The distribution of the ratio of correlated normal variables may be computed as

$$p\left(\hat{t}_f\right)=\int_{-\infty}^{\infty}\frac{p\left(-\hat{t}_f\hat{\beta}_1,\hat{\beta}_1\right)}{\left|-1/\hat{\beta}_1\right|}d\hat{\beta}_1, \tag{5}$$

where $p\left(\hat{\beta}_0,\hat{\beta}_1\right)$ is the bivariate normal distribution function. Eq. (5) is readily computed and has an analytical answer, but it is too cumbersome to write here. Because the exact population μ_j and σ_j are not known *a priori* and must be estimated from the data as presented above, a sampling distribution for the ratio mean and standard deviation should be derived, but in the present paper, the population ratio distribution, Eq. (5), will be used. It should be noted that this probability density function has no analytically-calculable order statistics, since the tails are too "fat" [18]. However, histograms of time-of-failure data may be compared to Eq. (5) to verify that the distribution of the data is appropriately modeled such that estimating order statistics from the data itself is reasonable.

CONCLUSIONS

Key objectives of this effort were to prove the viability of using FBG sensors in a fatigue loading environment and to assess the ability of the FBG sensors to support SHM system detection of damage and prognostics of structural life. An initial conclusion of the testing was that the FBG sensor arrays survived the fatigue environment and were still functional after undergoing 1.5M cycles on Panel1. The FBG sensor array was connected throughout the test on each of the specimens, with no indication of fatigue damage or wear-out of the sensor array or connections.

In addition, the previously developed SHM algorithm was successfully able to discern matrix damage to the laminate as well as the progression of the matrix damage in reducing the structural integrity. Figure 9 provided an example of the Mahalanobis distance metric demonstrating the ability of the SHM algorithm to discern damage to the panel and to indicate progression of the damage to the panel. Other pairs of sensors indicated similar behavior.

The success of the key objectives allowed for the population of a pool of data to be used for the development of a prognostics tool in predicting the life of a GRP part subjected to fully reversed cyclic fatigue loading. Once developed, the tool will be applied to a blind test specimen, with the data assessed

in real time to provide predictions of remaining life of the specimen under the prescribed loading.

ACKNOWLEDGMENTS

This material is based upon work supported by the Naval Sea Systems Command under Contract No. N00024-13-C-4053, SBIR N111-053. Any opinions expressed herein are those of the author(s) and do not necessarily reflect the views of the Naval Sea Systems Command.

REFERENCES

1. Sohn, H., et al., "Structural health monitoring using statistical pattern recognition techniques." Journal of dynamic systems, measurement, and control 123.4 (2001): 706-711.

2. Gul, M., and F. Necati Catbas, "Statistical pattern recognition for Structural Health Monitoring using time series modeling: Theory and experimental verifications." Mechanical Systems and Signal Processing 23.7 (2009): 2192-2204.

3. Kessler, S., et al., "Damage detection in composite materials using frequency response methods." Composites Part B: Engineering 33.1 (2002): 87-95.

4. Kersey, A., et al., "Fiber grating sensors." Journal of lightwave technology 15.8 (1997): 1442-1463.

5. De Oliveira, R., C. A. Ramos, and A. T. Marques. "Health monitoring of composite structures by embedded FBG and interferometric Fabry–Pérot sensors." Computers & structures 86.3 (2008): 340-346.

5. Majumder, M. et al., "Fibre Bragg gratings in structural health monitoring—Present status and applications." Sensors and Actuators A: Physical 147.1 (2008): 150-164.

6. Peters, K., "Full-spectrum FBG analysis of inhomogeneous, fast-varying strain effects." Asia Pacific Optical Sensors Conference. International Society for Optics and Photonics, 2012.

7. Jang, B., et al., "Detection of impact damage in composite structures using high speed FBG interrogator." Advanced Composite Materials 21.1 (2012): 29-44.

8. Park, S., T. Park and K. Han., "Real-time monitoring of composite wind turbine blades using fiber Bragg grating sensors." Advanced Composite Materials 20.1 (2011): 39-51.

9. Murayama, H., et al., "Structural health monitoring of a full-scale composite structure with fiber-optic sensors." Advanced Composite Materials11.3 (2002): 287-297.

10. Yeager, M. and M. Todd, “Binary Hypothesis-Based Impact Damage Detection for Composite Material System Embedded with Fiber Bragg Gratings,” (2015).

11. Voight, B, “A Method of Prediction for Volcanic Eruptions,” Nature 232: 125-130, 1988.

12. Voight B., “A Relation to Describe Rate-Dependent Material Failure,” Science 243: 200–203, 1989.

13. Boue, A., Lesage, P., Cortes, G., Valette, B., and Reyes-Davila, G. A., “Real-time Eruption Forecasting Using the Material Failure Forecast Method with a Bayesian Approach,” J. Geophysical Research 120: 2143–2161, 2015.

14. Bell, A. F., Naylor, M., Heap, M. J., and Main, I. G., :Forecasting Volcanic Eruptions and Other Material Failure Phenomena: An Evaluation of the Failure forecast method,” Geophysical Research Letters 38: L15304A, 2011.

15. Vasseur, J., Wadsworth, F., Lavallee, Y., Bell, A. F., Main, I. G., and Dingwell, D. B., “Heterogeneity: The Key to Failure Forecasting,” Nature Scientific Reports 5: 13259, 2015.

16. Kilburn, C. R. J. and Voight, B., “Slow Rock Fracture as Eruption Precursor at Soufriere Hills Volcano, Montserrat,” Geophysical Research Letters 25: 3665, 1998.

17. Corcoran, J., “Rate-Based Structural Health Monitoring Using Permanently Installed Sensors,” Proceedings of the Royal Society A 473: 20170270, 2017.

18. Hinckley, D. V., “On the Ratio of Two Correlated Normal Random Variables,” Biometrika 56(3): 635-639, 1969.